

NO-A102 071

MECHANISTIC UNDERSTANDING OF POWDER COMPACTION IN
METALS(U) CORNELL UNIV ITHACA NY DEPT OF MATERIALS
SCIENCE AND ENGINEERING R RAJ 25 JUN 87

1/1

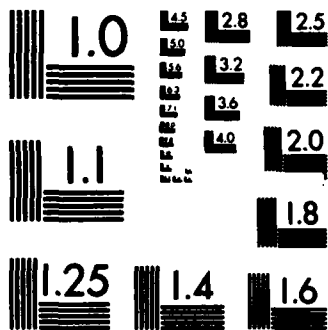
UNCLASSIFIED

AFOSR-TR-87-0916 AFOSR-84-0133

F/G 11/6.1

NL

					END							
					8-87							
					DTK							



MICROCOPY RESOLUTION TEST CHART
NATIONAL BUREAU OF STANDARDS-1963-A

AD-A182 871

DTIC ELECTED JUL 29 1987

REPORT DOCUMENTATION PAGE

1a. REPORT SECURITY CLASSIFICATION Unclassified		1b. RESTRICTIVE MARKINGS	
a. SECURITY CLASSIFICATION AUTHORITY		3. DISTRIBUTION / AVAILABILITY OF REPORT Unlimited	
b. DECLASSIFICATION / DOWNGRADING SCHEDULE		5. MONITORING ORGANIZATION REPORT NUMBER(S) AFOSR-TR-87-0916	
1. PERFORMING ORGANIZATION REPORT NUMBER(S) Not applicable		7a. NAME OF MONITORING ORGANIZATION Dr. A. H. Rosenstein	
2a. NAME OF PERFORMING ORGANIZATION Cornell University	6b. OFFICE SYMBOL (if applicable)	7b. ADDRESS (City, State, and ZIP Code) AFOSR 410 Bolling Air Force Base, Solid State Div. Washington, D.C. 22209	
3c. ADDRESS (City, State, and ZIP Code) Ithaca, NY 14853		9. PROCUREMENT INSTRUMENT IDENTIFICATION NUMBER AFOSR-84-0133	
4a. NAME OF FUNDING / SPONSORING ORGANIZATION AFOSR	8b. OFFICE SYMBOL (if applicable)	10. SOURCE OF FUNDING NUMBERS	
8c. ADDRESS (City, State, and ZIP Code) 410 Bolling Air Force Base Washington, D.C. 22209		PROGRAM ELEMENT NO. 611021	PROJECT NO. 2306
		TASK NO. A1	WORK UNIT ACCESSION NO.
11. TITLE (Include Security Classification) Final Report: Mechanistic Understanding of Powder Compaction in Metals			
12. PERSONAL AUTHOR(S) Raj, Rishi			
13a. TYPE OF REPORT Final--Grant	13b. TIME COVERED FROM 4/1/84 TO 1/30/86	14. DATE OF REPORT (Year, Month, Day) 87, 6, 25	15. PAGE COUNT
16. SUPPLEMENTARY NOTATION			
17. COSATI CODES		18. SUBJECT TERMS (Continue on reverse if necessary and identify by block number)	
FIELD	GROUP	Intermetallics, powder compaction, densification, sinter forging	
	SUB-GROUP		
19. ABSTRACT (Continue on reverse if necessary and identify by block number)			
Powder compacts of nickel aluminide were compressed under uniaxial load above 1373 K, in a way such that the material was free to move in the lateral direction. Lateral and axial displacements were measured by means of three LVDTs. The data so obtained gave a full description of the applied stress state and the strain state as a function of time during the flow and densification process. That allowed us to obtain simultaneous measurements of the time dependent, and density dependent shear and densification behavior of the powder compact. The shear rate was non-linear in stress suggesting a dislocation flow mechanism. A model for densification by power law creep was applied to the data. It greatly overestimated the measured densification rates. Interestingly it was found that it is difficult to densify the powder to a density of greater than about 0.80 (relative) by means of uniaxial compression. Further experiments were done where the powder was hot-pressed in a constraint cavity. In this case large hydrostatic pressures could be applied to the specimen and near theoretical densities were obtained, presumably because the			
20. DISTRIBUTION / AVAILABILITY OF ABSTRACT <input checked="" type="checkbox"/> UNCLASSIFIED/UNLIMITED <input type="checkbox"/> SAME AS RPT <input type="checkbox"/> DTIC USERS		21. ABSTRACT SECURITY CLASSIFICATION	
22a. NAME OF RESPONSIBLE INDIVIDUAL Rosenstein		22b. TELEPHONE (Include Area Code) 302-767-4931	22c. OFFICE SYMBOL DC

19. Abstract continued

hydrostatic pressure promoted the diffusional transport mechanism of densification. The hot-pressing data was combined with the sinter forging data to obtain the correlation between densification rate and applied pressure. The diffusional mechanism of densification gave good quantitative explanation for the densification behavior. In a broader context, we believe that powder consolidation techniques should be optimized with a view to both shear strain as well as hydrostatic pressure. The shear strain can promote microstructure refinement through dynamic recrystallization, while pressure provides a driving force for diffusional densification.

Accession For	
NTIS CRA&I	<input checked="" type="checkbox"/>
DTIC TAB	<input type="checkbox"/>
Unannounced	<input type="checkbox"/>
Justification	
By	
Distribution /	
Availability Codes	
Dist	Avail and/or Special
A-1	



AFOSR-TR- 87-0916

FINAL TECHNICAL REPORT

(4/1/84-11/30/86)

MECHANISTIC UNDERSTANDING OF POWDER COMPACTION IN METALS

AFOSR-84-0133

Prepared for: Air Force Office of Scientific Research
410 Bolling Air Force Base
Solid State Division
Washington, DC 22209
Attn: Dr. A. H. Rosenstein

Prepared by: Professor Rishi Raj
Department of Materials Science and Engineering
Cornell University
Ithaca, NY 14853-1501

June 1987

ABSTRACT

Powder compacts of nickel aluminide were compressed under uniaxial load above 1373 K, in a way such that the material was free to move in the lateral direction. Lateral and axial displacements were measured by means of three LVDTs. The data so obtained gave a full description of the applied stress state and the strain state as a function of time during the flow and densification process. That allowed us to obtain simultaneous measurements of the time dependent, and density dependent shear and densification behavior of the powder compact. The shear rate was non-linear in stress suggesting a dislocation flow mechanism. A model for densification by power law creep was applied to the data. It greatly overestimated the measured densification rates. Interestingly it was found that it is difficult to densify the powder to a density of greater than about 0.80 (relative) by means of uniaxial compression. Further experiments were done where the powder was hot-pressed in a constraint cavity. In this case large hydrostatic pressures could be applied to the specimen and near theoretical densities were obtained, presumably because the hydrostatic pressure promoted the diffusional transport mechanism of densification. The hot-pressing data was combined with the sinter forging data to obtain the correlation between densification rate and applied pressure. The diffusional mechanism of densification gave good quantitative explanation for the densification behavior. In a broader context, we believe that powder consolidation techniques should be optimized with a view to both shear strain as well as hydrostatic pressure. The shear

strain can promote microstructure refinement through dynamic recrystallization, while pressure provides a driving force for diffusional densification.

INTRODUCTION

The availability of high temperature ceramic fibers may lead to the development of a new class of metal-matrix structural composites. The fibers will impart high modulus and where the metal has limited ductility, as is often the case with intermetallic compounds, they may also increase toughness and reliability.

Metal matrix composites will almost certainly be fabricated by powder metallurgy techniques. The present paper is an attempt to develop experimental and analytical tools for the optimization of a special kind of a compaction process which we call sinter forging. The idea is akin to the isothermal forging process used in shaping nickel-base and titanium alloys, except that in sinter forging the workpiece is a porous powder compact. Thus the forging process while imparting shape, is also used to densify the compact to near full density.

At the fundamental level, the sinter forging process involves both densification strain, as well as effective or shear strain. If the sinter forging process were to be numerically simulated it would be necessary to have constitutive equations for both shear and densification behavior of the material. These constitutive equations

will depend not only on strain rate and temperature but also on density which will be an evolutionary parameter in the problem.

In the current paper we present a simple technique for measuring the rate dependent shear and densification constitutive equations for powder compacts. The same technique was applied earlier to ceramic materials (1). Here we use it to study a metal, specifically the nickel-aluminide intermetallic. The technique consists of uniaxial pressing of the powder without any lateral constraint at high temperatures. The axial as well as the radial strains are measured which provide a full description of the stress and strain tensor as a function of time. A limitation of this technique is that the hydrostatic pressure cannot be greater than the yield stress of the material.

In addition to sinter forging we also carried out hot-pressing experiments where the powder is pressed in an enclosed die. In this case nearly full density was obtained because the die constraint allows the application of hydrostatic pressure which is greater than the yield stress. While, the results of the hot-pressing experiments by themselves are difficult to analyze because the die wall pressure is unknown, the flow properties of the material measured from the sinter forging experiment allowed us to estimate the wall pressure and reach an understanding of the densification mechanisms. It was concluded that diffusional transport contributed significantly in the final stages of densification.

The theoretical studies of powder compaction have been largely concerned with the removal of pores. Matrix deformation and

diffusional transport are two distinct mechanisms by which matter can be transported to fill the pores. Both mechanisms have been studied in detail and equations developed from them have been expressed in the form of maps (2). In this approach plastic strain only serves the purpose of pore removal since the applied stress is purely hydrostatic. Plastic deformation stops when the material is fully dense. Thus the average plastic strain experienced by the material during the densification process is of the same order as the maximum volumetric strain, which will be equal to $\ln(1/\rho_0)$ where ρ_0 is the initial density of the workpiece. For example if $\rho_0 = 0.6$ then the maximum plastic strain will be of the order of 0.50.

Plastic or dislocation strain in hot-working is frequently used to refine the microstructure. Dynamic recrystallization is an obvious example of grain refinement (3) where a critical amount of shear strain is required to achieve grain refinement, but in addition, dislocation hardening can lead to boundary migration which can serve to ameliorate the brittle properties of prior particle grain boundaries. The inference is that the magnitude of the shear strain must be included as one of the criteria in the optimization of the powder consolidation process. This also means that hot-isostatic-pressing by itself may not be enough to obtain the best properties; HIP should be followed by deformation processing to induce grain refinement. Instead, a sinter forging process can be used to obtain densification, shear strain, and net-shape in one step. The design of the sinter forging process requires the knowledge of the constitutive equations for densification and shear of porous materials. This paper describes a technique for

obtaining such equations. A good review of the state-of-art status of powder metallurgy processing can be found in Ref. 4.

EXPERIMENTAL TECHNIQUE

Definition of Stress and Strains

We assume that the principal stresses and strains are known and they are:

$$[\sigma] = \begin{matrix} \sigma_1 & 0 & 0 \\ 0 & \sigma_2 & 0 \\ 0 & 0 & \sigma_3 \end{matrix} ; \quad [\epsilon] = \begin{matrix} \epsilon_1 & 0 & 0 \\ 0 & \epsilon_2 & 0 \\ 0 & 0 & \epsilon_3 \end{matrix} \quad [1]$$

where σ_i are the principal stresses and ϵ_i are the principal strains. Both are defined to be positive if they are tensile. The shear components can then be defined by the effective stress and strain, σ_e and ϵ_e , as follows:

$$\sigma_e = \sqrt{1/2 \{(\sigma_1 - \sigma_2)^2 + (\sigma_2 - \sigma_3)^2 + (\sigma_3 - \sigma_1)^2\}}$$

and

[2]

$$\epsilon_e = \frac{2}{3} \sqrt{1/2 \{(\epsilon_1 - \epsilon_2)^2 + (\epsilon_2 - \epsilon_3)^2 + (\epsilon_3 - \epsilon_1)^2\}}$$

The numerical factors in Eq. [2] are such that σ_e and ϵ_e are equal to the uniaxial quantities in a simple uniaxial test.

The volumetric quantities are pressure, p , and the strain, ϵ_a , which are given by:

$$p = -(\sigma_1 + \sigma_2 + \sigma_3)/3$$

$$\epsilon_a = \epsilon_1 + \epsilon_2 + \epsilon_3$$
[3]

Note that ϵ_a in Eq. [3] will have negative sign if the workpiece reduces in volume as a result of densification.

The strain equations in [2,3] are also valid for strain rates.

The Technique

The technique used to measure all the principal stress and strains is shown schematically in Fig. 1. A cylindrical workpiece is compressed between two pistons without any lateral constraint. The axial as well as the radial displacements are measured. The radial displacement is determined by taking the average of measurements of two LVDTs placed diametrically opposite to each other. Let us assume that the axial stress is σ_z , and that the friction between the pistons and the workpiece is negligible, which means that the other two principal stresses are equal to zero. The corresponding principal strains are ϵ_z , ϵ_r , and ϵ_r , where the radial strains are assumed to be equal, that is, flow and densification are assumed to be isotropic in the lateral plane. Substitution of these quantities in Eqs. [2] and [3] leads to the following equations:

$$p = -\sigma_z/3 ,$$

$$\epsilon_a = \epsilon_z + 2\epsilon_r ,$$

$$\sigma_e = |\sigma_z| ,$$

$$\text{and, } \epsilon_e = \frac{2}{3}|\epsilon_z - \epsilon_r|$$
[4]

Materials

The model material chosen for this study was a nickel aluminide having the composition $\text{Ni}_{.64}\text{Al}_{.36}$. The non-equimolar composition leads to self diffusion coefficients which are more than two orders of magnitude faster than those for the equimolar composition (5). The relative rate of diffusion of nickel and aluminum at this composition differs by less than a factor of 1.25; thus diffusional transport should not give rise to significant segregation. The powders were prepared by the rotating electrode technique which gives nearly spherical particles. Particles were separated by 500 mesh screen; the average particle size in the powder as determined by scanning electron microscopy was 25 μm .

The above composition of nickel-aluminide separates into δ and ϵ phases at room temperature. The exact theoretical density of these constituent phases at room temperature was calculated using the lattice parameter data as a function of composition provided in Ref. 6. This gave a density of 6.50 gm cm^{-3} for the δ phase and 7.31 gm cm^{-3} for the ϵ phase. The relative amounts of the two phases for our composition are predicted to be 96.8% of the δ phase and 3.2% of the ϵ phase from the phase diagram. Thus the ideal theoretical density of the material at room temperature is predicted to be 6.52 gm cm^{-3} .

The sinter forging and hot-pressing experiments were all performed at 1373 K. At that temperature the equilibrium fractions of δ and ϵ phases are 90.6% and 9.4% respectively which leads to an average ideal density of 6.57 gm cm^{-3} .

Experiments

Specimens for sinter forging experiments were prepared by cold compaction of raw powder in a cylindrical die up to a pressure of 2.5 MPa. The specimens obtained from cold pressing were hot-pressed in a graphite die at 1223 K at a pressure of 5 MPa for a period of 20 to 25 min after reaching the hot-pressing temperature. This procedure yielded specimens for sinter forging which were 12.7 mm in diameter and varied in height from 17.2 mm to 19.0 mm. Their density varied from 0.68 to 0.72 of the theoretical density.

The sinter forging experiments were carried out at 1373 K by compressing the specimens prepared as above between flat faced pistons of high purity graphite in a vacuum of 10^{-5} torr. The heat up schedule consisted of heating up to 473 K over a period of 10 min, holding at that temperature for ten minutes to allow outgassing, and then increasing the temperature to 1373 K linearly with time over a period of 45 min. The uniaxial load was applied after reaching 1373 K.

Altogether five sinter forging experiments were completed. Each was carried out at a fixed applied load which was kept constant throughout the test. The magnitudes of the five loads for the five experiments, expressed in terms of the initial uniaxial stress, were as follows: $\sigma_z^0 = -7.72$ MPa, -11.97 MPa, -18.04 MPa, -23.42 MPa, and -28.83 MPa. Since the cross-sectional area of the specimens increased with time the initial stresses represent the maximum value of the applied stress.

In addition to the sinter forging experiments, we also carried out five hot-pressing experiments. In this case the diameter of the

hot-pressing die was 12.7 mm and the inside die-wall was lined with graphoil of thickness 0.13 mm. The die was filled with powder by tapping. The initial height of the powder was approximately 12.7 mm. The same procedure as described in the preceding experiments was used for heating up to the hot-pressing temperature. The hot pressing loads used in the five tests corresponded to a compressive uniaxial stress of 8.5 MPa, 13.0 MPa, 17.9 MPa, 23.5 MPa, and 30.0 MPa.

Correction for Friction

The specimens showed some barrelling at the end of the sinter forging experiments because of finite friction between the workpiece and graphite pistons. Barrelling led to an error in the measurement of the radial strain. The error was corrected by estimating the effective diameter of the specimen at the end of the sinter forging experiment; this was obtained from the final height of the specimen and its total volume as measured by the Archimedes method. The correction was greater than 5% but always less than 10% of the total increase in the diameter of the specimen during sinter forging. The exact correction could be obtained only at the end point of the experiment and we were forced to make an assumption about the correction for the intermediate points during the forging test. The assumption was not too critical since the maximum correction to the radial strain was less than 10%. We assumed that the displacement correction increased linearly with time. The idea is illustrated in Fig. 2. The solid line shows the radial displacement as measured by the LVDTs. The straight line at the bottom of the figure gives the assumed correction and the dashed line,

which is the difference between these two curves, is assumed to be the corrected radial displacement.

The measurement of the specimen volume described in the previous paragraph needs to be discussed in more detail. Since the specimen contained at least some interconnected porosity, the Archimedes method was used in a slightly different way. The amount of fluid absorbed by the porous solid was obtained from the difference in the mass of the solid before and after its immersion in the fluid.

RESULTS AND ANALYSIS OF SINTER FORGING EXPERIMENTS

Shear Strain, Densification Strain and Applied Stress as a Function of Time

The radial and axial (true) strains calculated from the displacement measurements are plotted in Figs. 3 and 4. Each curve corresponds to one experiment carried out at a constant applied load. The magnitude of that load, expressed in terms of the initial axial stress is stated in the figures. It ranged from -7.7 MPa to -28.8 MPa. The axial strains at the end of the experiments ranged from -0.6 to -0.9, that is the final height of the specimens was 0.55 to 0.41 of their initial height. The radial strains were positive and ranged from 0.25 to 0.35. The rate of deformation was very sensitive to stress since it took 42 min to complete the test at -7.7 MPa but only 2 min at -28.8 MPa.

The true axial stress, σ_z , was calculated using the following equation:

$$\sigma_z = \sigma_z^0 e^{-2\epsilon_r} \quad [5]$$

The data in Fig. 4 and Eq. [5] led to the results shown in Fig. 5. The volumetric and the effective strains were obtained from the data presented in Figs. 3 and 4, and the use of Eqs. [4]. The results are given in Figs. 6 and 7. The effective strain represents shear and is therefore necessarily positive. The volumetric strain however, can be negative or positive. Negative volumetric strain implies densification of the powder compact whereas a positive volumetric strain would mean that the porosity is increasing due to fracture. The results in Fig. 7 show that the strain was always negative.

The relative density of the powder compact can be calculated from the volumetric strain. We define the relative density, ρ , such that when the compact is fully dense $\rho = 1$. The volumetric strain, ϵ_a , then, is related to the volume, V , the initial volume, V_0 , the density, ρ , and the initial density, ρ_0 by the following equation:

$$\epsilon_a = \ln\left(\frac{V}{V_0}\right) = \ln\left(\frac{\rho_0}{\rho}\right) \quad [6]$$

Here ρ_0 and V_0 are the quantities at the point when load was applied to the powder compact after reaching the sinter forging temperature. The measurement of the final density, and the maximum value of ϵ_z for each sinter forging experiment allows us to calculate ρ_0 from Eq. [6]. These results are presented in Table 1. They show the initial density to be approximately 0.69.

Note from Eq. [6] that the densification rate is related to the volumetric strain rate by the equation:

$$\frac{d \ln \rho}{dt} = \frac{\dot{\rho}}{\rho} = \dot{\epsilon}_a \quad [7]$$

Power-Law Creep

The effective stress, the effective strain rate, and the density can be related to each other through the data given in Figs. 4, 5, and 6. The data are cross-correlated by choosing a fixed time. Many sets of data are obtained by varying the time. Note that the effective stress is exactly equal to σ_z only if the friction is exactly zero. We know that it is not; but since we did not get severe barrelling and since the densification of the powder compact was quite uniform we will assume that the correction due to the friction was small. Also note that the density was obtained from the volumetric strain ϵ_a , the use of Eq. [6], and Table 1.

A reasonable indicator of the micromechanism of high temperature deformation is the stress exponent, n , in the constitutive equation:

$$\dot{\epsilon}_e = \dot{\epsilon}_o \left(\frac{\sigma_e}{\sigma_o} \right)^n \quad [8]$$

where $\dot{\epsilon}_o$ and σ_o are normalizing parameters. If n is equal to one then it is likely that diffusional creep is the operating mechanism, and if $n > 3$ then the more likely mechanism is power-law dislocation creep.

A logarithmic plot of the effective strain rate versus effective stress, at different densities is given in Fig. 8. The average slope

leads to stress exponent $n = 4.0$. We infer that within the constraints of the parameters used in our experiments, the material was deforming by dislocation creep. It is interesting to note in Fig. 8 that a small change in the density, a change from 0.68 to 0.76 increased the strain rate by more than a factor of ten. Clearly the effect of porosity on deformation rate is quite nonlinear.

Densification Behavior

The mechanism of pore closure is likely to be the same as the mechanism for shear deformation of the porous solid. The simple argument is that since the majority of the pores are situated at three grain junctions, the diffusion distance for diffusion mass transport is equal to one half of the grain size. For diffusional creep the diffusion distance is equal to the grain size. Thus, while a narrow window may exist where the overall deformation takes place by dislocation creep while pore closure occurs by diffusional flow, in general, both processes are likely to be controlled by the same mechanism. Therefore, we have compared our data to the results of a model by Banks-Sills and Budiansky (7) who considered the general problem of void collapse in nonlinear viscous solids under compressive loadings. Their results were computed numerically and we compare our data to their Figure 15.

The change in the volume of pores during deformation of a nonlinear viscous solid depends only on the stress exponent, the state of applied stress, and the applied strain. The magnitude of the applied stress is not important. The data can, therefore, be

normalized in terms of the applied plastic strain if the stress strain remains invariable. The present situation is a simple example of the treatment by Banks-Sills and Budiansky. Their numerical results are presented as the change in the volume of the pores with applied uniaxial strain for different values of n , the power law stress exponent. By suitable manipulation of Eq. [6] it can be shown that ϵ_a is related to the change in the volume of the pores, v/v_0 , as following:

$$\epsilon_a = \ln \left\{ \rho_0 + \frac{v}{v_0} (1 - \rho_0) \right\} \quad [9]$$

where v_0 is the initial volume of the pores and v is the current volume. In Eq. [9], ρ_0 is the density of the specimen at the start of the sinter forging experiment. For the present experiments (please refer to Table 1) we assumed that $\rho_0 = 0.69$. The numerical results given by Banks-Sills and Budiansky were converted into volumetric strain ϵ_a by Eq. [9]. The theoretical prediction for the relationship between ϵ_a and ϵ_z , for $n=4$ and $\rho_0 = 0.69$, is shown by the solid curve in Fig. 9. The experimental points obtained by correlating data from Figs. 3 and 7, for all five sinter forging tests are shown on the same graph. Although the theoretical and experimental curves show the same shape, that is the rate of pore closure with axial strain increases with increasing axial strain, there is a wide discrepancy between the magnitude of the rate of pore closure. The absolute rate is much slower than predicted by theory. We cannot give a satisfactory explanation for this discrepancy at the present time except to point

out that a similarly large gap between theory and experiment was found by McClintock when he compared his theory for pore growth (8) under tensile strain with experiment (9). The answer does not lie in the theoretical assumption in the analysis (7) that the pores are completely isolated from their neighbors since interaction between the flow fields of adjacent pores would serve to increase the rate of pore closure, which will further increase the discrepancy between theory and experiment.

RESULTS AND ANALYSIS OF HOT-PRESSING EXPERIMENTS

In a hot-pressing experiment the radial strain is zero since the lateral displacement is constrained by the die wall. Thus the strain tensor is completely described by the axial strain ϵ_z ; all other strain components are zero. The stress tensor is more complicated because the radial stress imposed by the die wall is an unknown quantity. The principal stresses are, therefore, σ_z which is known since it is equal to the applied uniaxial stress, and the two radial stress components, σ_r , which are equal to each other but are an unknown quantity. Substitution of these principal stresses and strains into equations [2], and [4] leads to the following results for the effective and mean stresses and strains for the hot-pressing experiment.

$$p = -1/3(\sigma_z + 2\sigma_r) \quad (a)$$

$$\epsilon_a = \epsilon_z \quad (b)$$

$$\sigma_e = |\sigma_z - \sigma_r| \quad (c)$$

$$\text{and } \epsilon_e = 2/3|\epsilon_z| \quad (d)$$

[10]

Since σ_r is unknown the results from hot-pressing experiments cannot be unambiguously interpreted. In the present situation, however, the data from sinter forging experiments can be used to estimate σ_r . The procedure consists of estimating the effective stress, σ_e for a given strain rate $\dot{\epsilon}_e$ from sinter forging data such as that presented in Fig. 8. The effective strain rate is well defined in the hot-pressing experiment by Eq. [10d]. The substitution of the effective stress, which is estimated from the sinter forging experiments, into Eq. [10c] gives the value for σ_r . This value of σ_r can then be substituted in Eq. [10a] to calculate the pressure which is driving the densification rate given by Eq. [10b]. The power law relationship between the pressure and the densification rate can then be used to determine whether or not pore closure is being controlled by the diffusional mechanism. In the following section we present the results of such an analysis.

The basic data obtained from the hot-pressing experiments in the current study are shown in Fig. 10. The quantity L_z^f refers to the theoretical limit of the specimen height if it were fully dense, while L_z refers to the specimen height as measured during the hot-pressing experiment. We note from the data that except for the case of the lowest σ_z , the specimens were allowed to reach their full density before the test was ended. This is in sharp contrast to the sinter forging experiments where the final density of the specimens was less than 80%. An immediate inference from this observation is that the die wall was exerting a large hydrostatic stress on the specimen which enhanced the rate of densification of the powder compact.

The data in Fig. 10 allows us to calculate $\dot{\epsilon}_z$, and from that we can obtain ϵ_e and ϵ_a with the use of Eqs. [10b and d]. Note that in a hot-pressing experiment ϵ_e is always equal to two-thirds of ϵ_a . The result showing $\dot{\epsilon}_a$ and $\dot{\epsilon}_e$ as a function of σ_z are shown in Fig. 11, for four different values of density.

In order to understand the densification mechanism it is necessary to obtain the magnitude of the applied pressure. This can be done by calculating the effective stress from Fig. 8 and then substituting that in the following equation:

$$p = -\sigma_z - 2/3 \sigma_e \quad [11]$$

Equation [11] is valid only for the hot-pressing experiment and is derived by eliminating σ_r from Eqs. [10a and c]. The effective stress for the strain rate data in Fig. 11 was obtained by transposing that data to Fig. 8. The magnitudes of the effective stress so obtained are shown in Fig. 12. When the effective stress values, obtained from Fig. 12, are substituted in Eq. [11] and the pressure is plotted against the volumetric strain rate then the graph shown in Fig. 13 is obtained. Note that the volumetric strain rate for the hot-pressing experiment is always equal to 1.5 times the effective strain rate.

The data described in Fig. 13 can be used to interpret the mechanism of densification. At the lower stress the slope of the pressure vs densification curves approaches unity which is suggestive of the diffusional mechanism. Since the density values are quite high we may assume that the densification is in its final stage where the pores are isolated from each other and are placed at three grain

junctions. If that is the case then the questions developed for pore growth in creep rupture experiments should be applicable here. We consider equation [C2] in Ref. 11. In that equation we assume that the pores have spherical geometry and that they are located at three grain junctions; then the parameter $r_b^2/4\ell^2$ in equation [C2] becomes equal to the volume fraction of pores in the material, that is, $(1-\rho) = r_b^2/4\ell^2$. Since the particle size in our specimens was equal to 25 μm the rate controlling mechanism for diffusion transport is likely to be lattice diffusion rather than boundary diffusion; therefore, we replace $\pi\delta D_b$ in equation [C2] by dD_L , where d is the grain size and D_L is the lattice diffusion coefficient. The left hand side of the equation in [C2] is the rate of change of pore volume with time. If we assume the grain volume to be equal to d^3 then we can show that the left hand side of the equation is equal to $\dot{\epsilon}_a \times d^3$. With these substitutions we obtain the following equation for the volumetric strain rate:

$$\dot{\epsilon}_a = - \frac{2\pi D_L}{d^2} \frac{p\Omega}{kT} \frac{[1 - 4(1-\rho)]}{\frac{1}{2} \ln \frac{1}{4(1-\rho)} - \frac{3}{4} + 4\rho(1-\rho)} \quad [12]$$

Here p is the externally applied mean pressure to the powder compact, and Ω is the average atomic volume of diffusion.

The dashed theoretical line in Eq. [13] was obtained from Eq. [12] after the following substitutions: $D_L = 4 \times 10^{-13} \text{ m}^2 \text{ s}^{-1}$ (from diffusion data given in Ref. 2), $\rho = 0.94$, $d = 25 \mu\text{m}$, $T = 1373 \text{ K}$, $k = 1.38 \times 10^{-23} \text{ JK}^{-1}$, and $\Omega = 1.21 \times 10^{-29} \text{ m}^3$ (calculated assuming a density of 6.53 gm cm^{-3} , and a stoichiometry of $\text{Ni}_{.64}\text{Al}_{.36}$). It must be

considered remarkable that the theoretical prediction comes within a factor of two of the densification data. At the very least, this suggests that the experimental technique described in this paper should be pursued further to study the mechanisms and constitutive equation for flow and densification of porous metallic and ceramic bodies where linear and nonlinear viscous mechanisms may be operating.

CONCLUDING REMARKS

Powder methods are coming into increasing use for the fabrication of interesting new materials. Metal-matrix/ceramic fiber composites and mechanically alloyed aluminum are examples of materials which must be processed by powder technology.

Most of the theoretical work in powder consolidation has concentrated on the hot-isostatic-pressing technique where the pore shrinkage is the major concern. A case can be made, however, for also including shear strain as one of the criteria in the optimization of the densification process. The reason is that not only must the pores be removed but the material should also be subjected to a critical amount of shear strain in order to bring about phenomena which refine or improve the microstructure. Examples are dynamic recrystallization, removal of the prior particles grain boundaries, and the removal of large defects in the cold pressed microstructure.

The analytical and experimental techniques presented in this paper offer a methodology for developing constitutive equations which describe the densification as well as the shear behavior of powder

compacts. Some problems remain, especially the problem of friction between the die and the workpiece, but in general the approach seems promising. The fundamental information obtained from such experiments can then be used in process simulation of sinter forging method for net shape forming from powder starting materials.

ACKNOWLEDGMENTS

This research was supported by the Air Force Office of Scientific Research under Grant No. AFOSR-84-0133, under the direction of Dr. A. H. Rosenstein. Support was also received from the National Science Foundation through the use of the facilities of the Materials Science Center at Cornell University.

REFERENCES

1. K.R. Venkatachari and R. Raj, *J. Amer. Ceram. Soc.*, Vol. 69, 499-506 (1986).
2. F. Arzt, M.F. Ashby and K.E. Easterling, *Metall. Trans. A*, Vol. 14A, 211 (1983).
3. J.J. Jonas and M.J. Luton, Advances in Deformation Processing, Eds. J.J. Burke and V. Weiss, Plenum, NY (1978), pp. 215-243.
4. Powder Metallurgy Processing, Eds. H.A. Kuhn and A. Lawley, Acad. Press, NY (1978).
5. S. Shankar and L.L. Seigle, *Metall. Trans. A*, Vol. 9A, 1467 (1978).
6. Handbook of Lattice Spacings and Structure of Metals, W.B. Pearson, Vol. 1 and 2, Pergamon Press, NY (1958, 1967).
7. L. Banks-Sills and B. Budiansky, *Mech. of Mater.*, Vol. 1, 209-218 (1982).
8. F.A. McClintock, *J. Appl. Mech.*, Vol. 35, p. 363 (1965).
9. B.I. Edelson and W.M. Baldwin, Jr., *Trans. ASM*, Vol. 65, p. 230 (1962).
10. R. Raj, H.M. Shih and H.H. Johnson, *Scripta Metall.*, Vol. 11, 839-842 (1977).

Table I

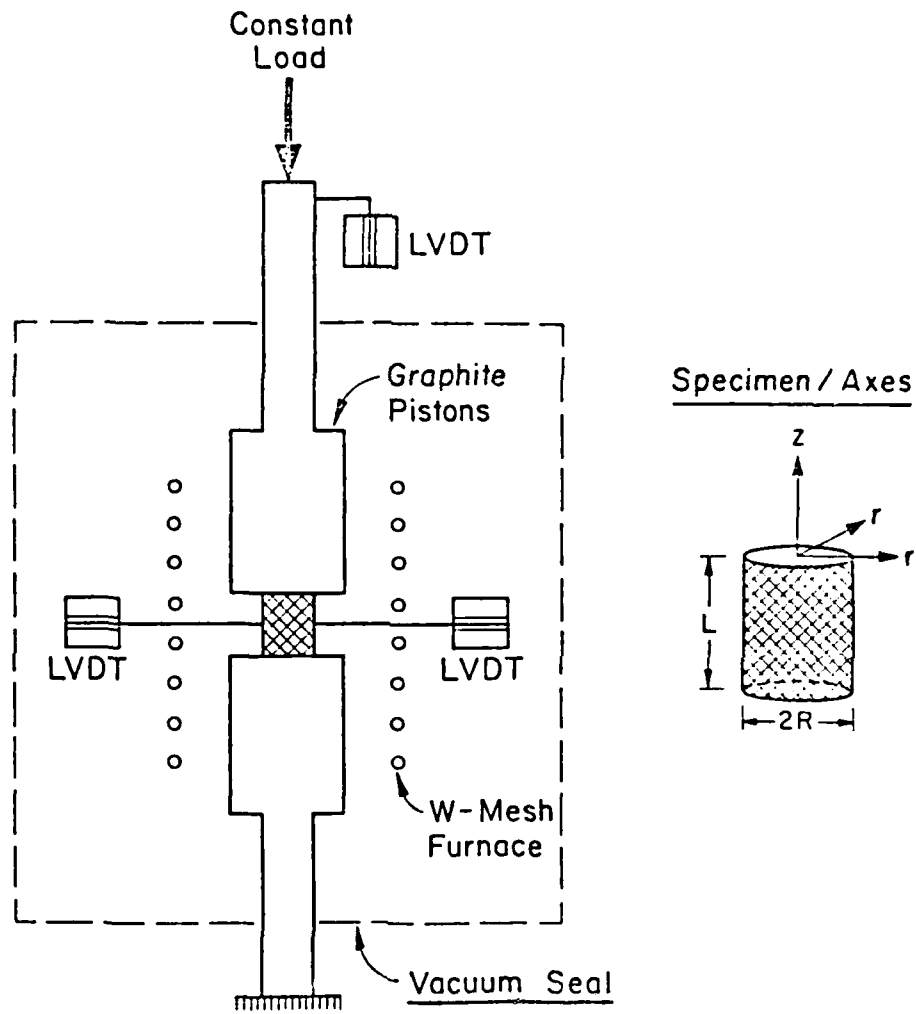
The initial value of the applied stress for the five sinter forging experiments. ρ_{final} is the density obtained at the end of each experiment and ρ_0 is the extrapolated density of the material at the point of application of the uniaxial load.

σ_z^0 (MPa)	ρ_{final}	ρ_0
-7.7	0.779	0.696
-12.0	0.782	0.687
-18.0	0.780	0.678
-23.4	0.773	0.686
-28.8	0.789	0.698

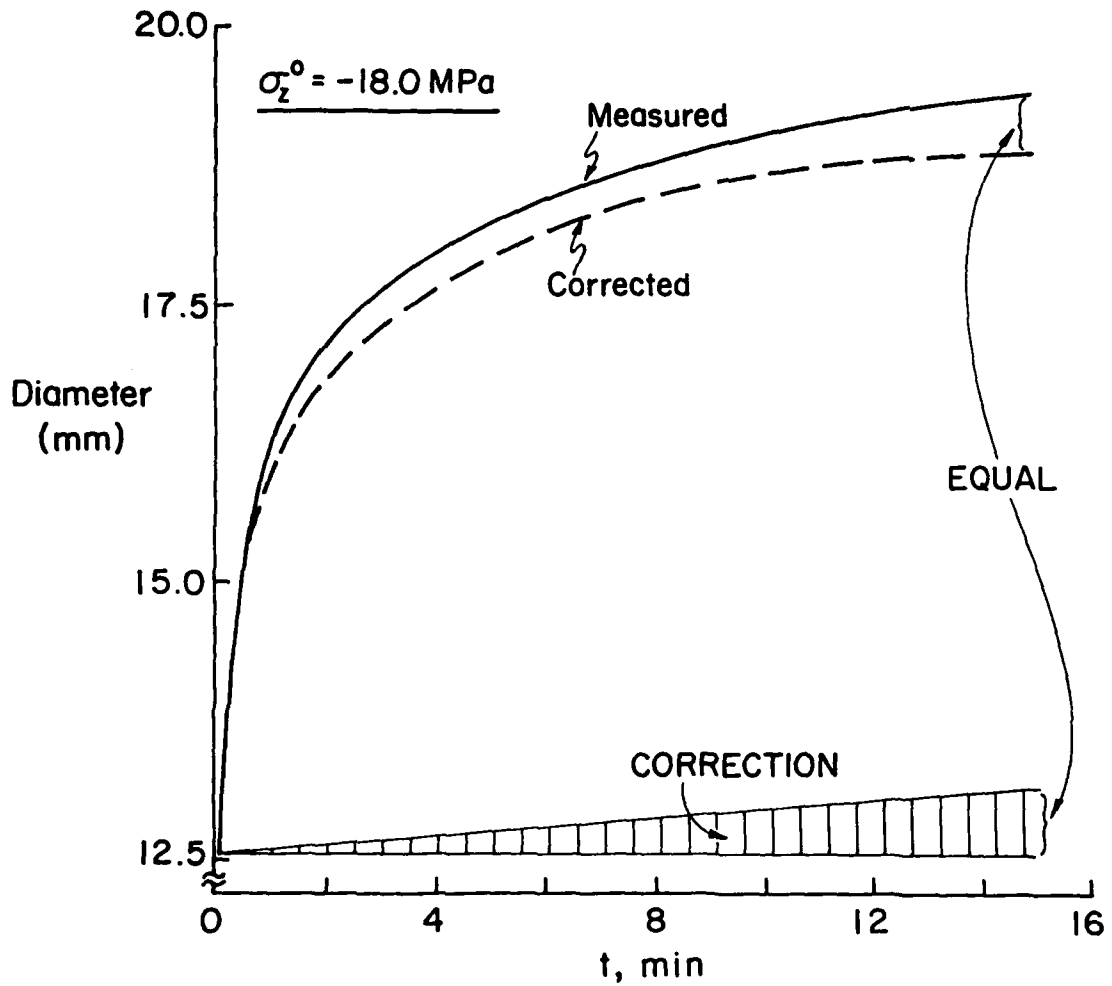
FIGURE CAPTIONS

1. A schematic illustration of the technique used to measure radial and axial strains in the sinter forging experiments. (Courtesy American Ceramic Society, Reference 1.)
2. The procedure used to account for error in the measurement of the radial strain as a result of barrelling. The correction at the end point of the experiment is exact. In the intermediate region a linear extrapolation is assumed.
3. The axial strain as a function of time for the five sinter forging experiments. The stress is equal to the initial value of the applied stress, σ_z^0 . The experiments were carried out at constant load.
4. The radial strain as a function of time for the five sinter forging experiments. The stress is equal to the initial value of the applied stress, σ_z^0 . The experiments were carried out at constant load.
5. The true stress experienced by the specimens during the course of the five sinter forging experiments. The experiments were carried out at constant load.
6. The effective strain, ϵ_e , as a function of time for the five sinter forging experiments.

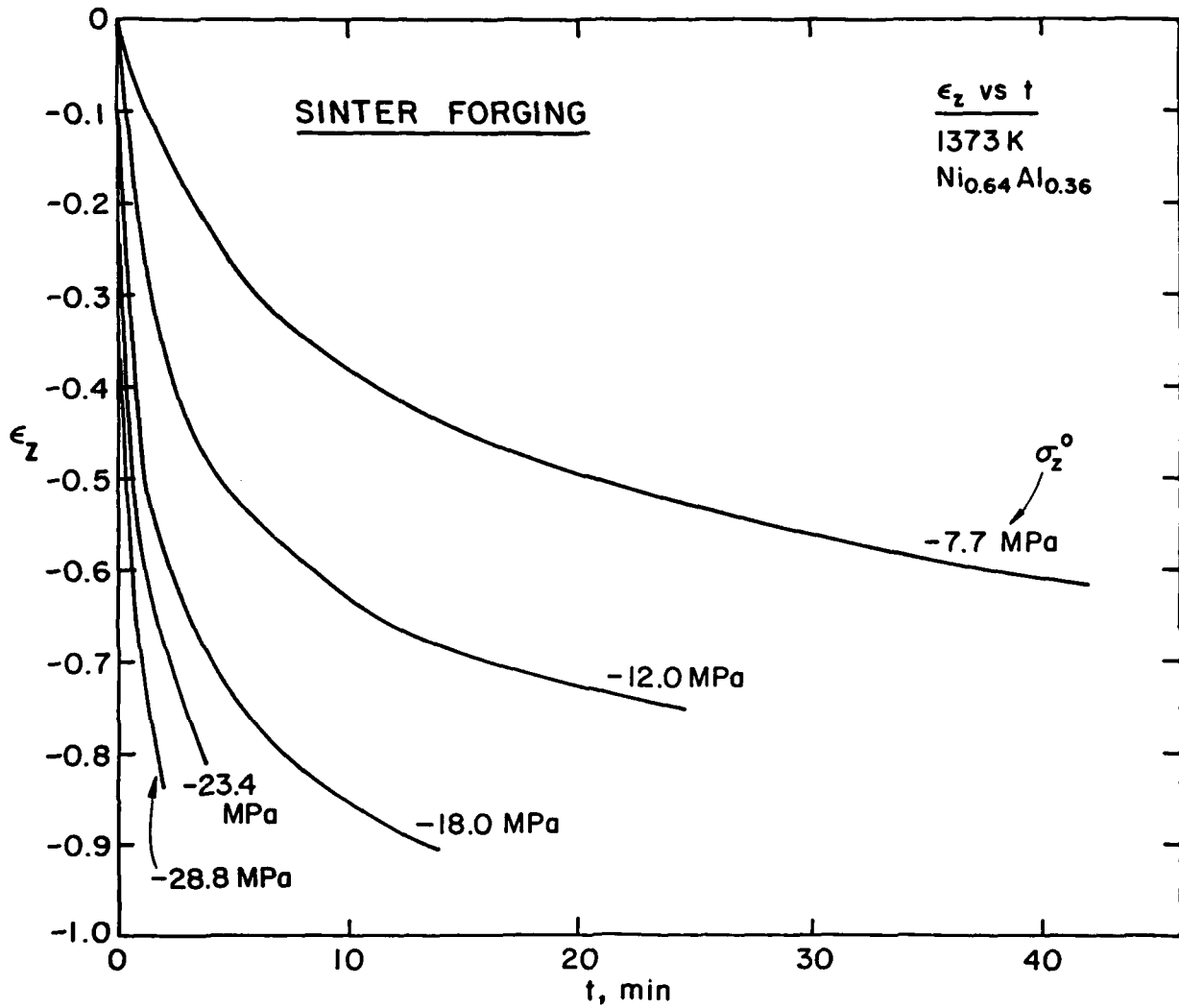
7. The volumetric strain, ϵ_a , as a function of time for the five sinter forging experiments.
8. A logarithmic plot of $\dot{\epsilon}_e$ and σ_e to determine the value of the stress exponent for power law creep.
9. A comparison between the theoretical prediction and the measured rate of pore closure with applied axial strain. The theory greatly overestimated the closure rate of the pores.
10. Data obtained from the five hot-pressing experiments. In hot-pressing the applied uniaxial stress remains constant since the specimen diameter does not change.
11. A plot of $\dot{\epsilon}_e$ and $\dot{\epsilon}_a$ as a function of the uniaxial stress, σ_z . Note that the $\dot{\epsilon}_e$ is always two-thirds of $\dot{\epsilon}_a$.
12. The procedure used for obtaining the effective stress σ_e for the hot-pressing experiments by using $\sigma_e \sim \dot{\epsilon}_e$ data obtained from sinter forging experiments.
13. A plot of the volumetric strain rate $\dot{\epsilon}_a$ versus the applied pressure for hot-pressing experiments, and a comparison between theoretical prediction and experimental results.



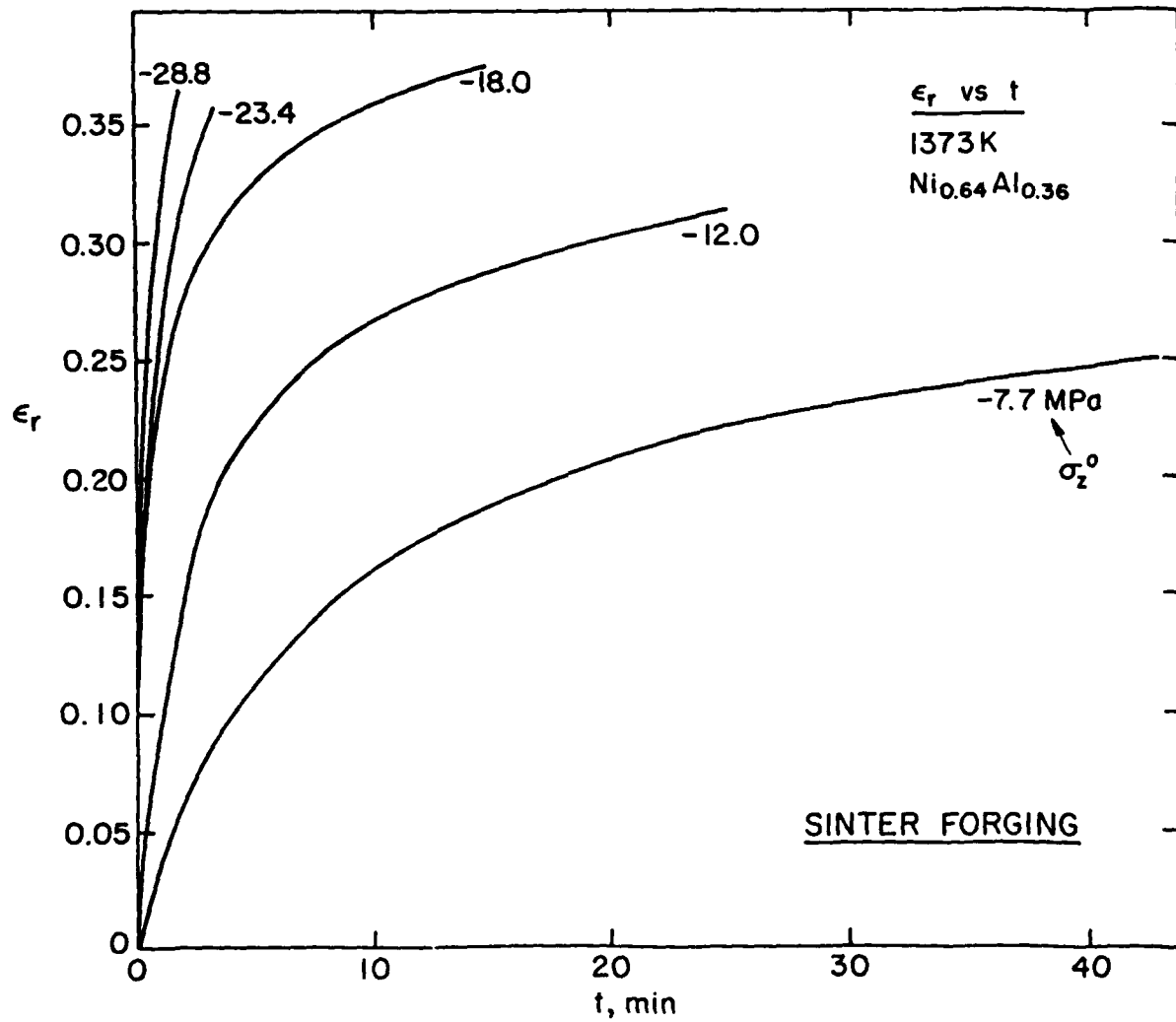
1. A schematic illustration of the technique used to measure radial and axial strains in the sinter forging experiments. (Courtesy American Ceramic Society, Reference 1.)



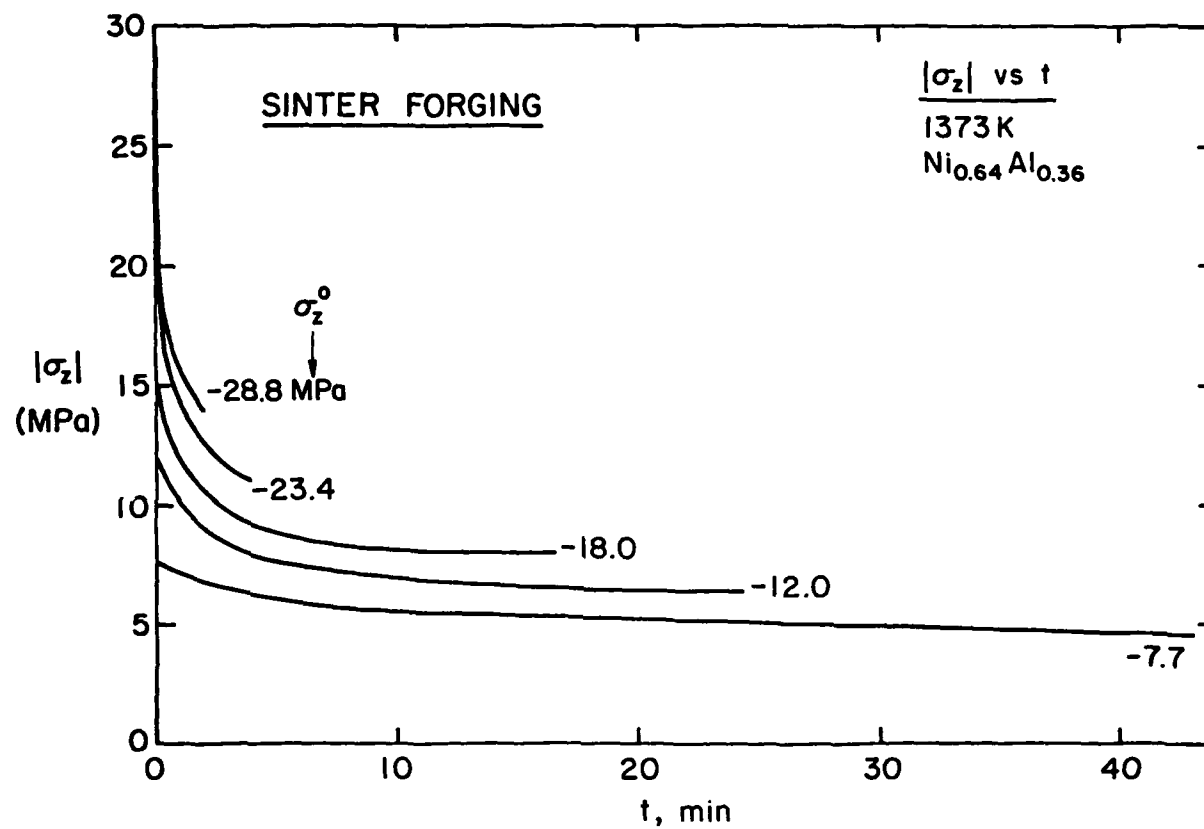
2. The procedure used to account for error in the measurement of the radial strain as a result of barrelling. The correction at the end point of the experiment is exact. In the intermediate region a linear extrapolation is assumed.



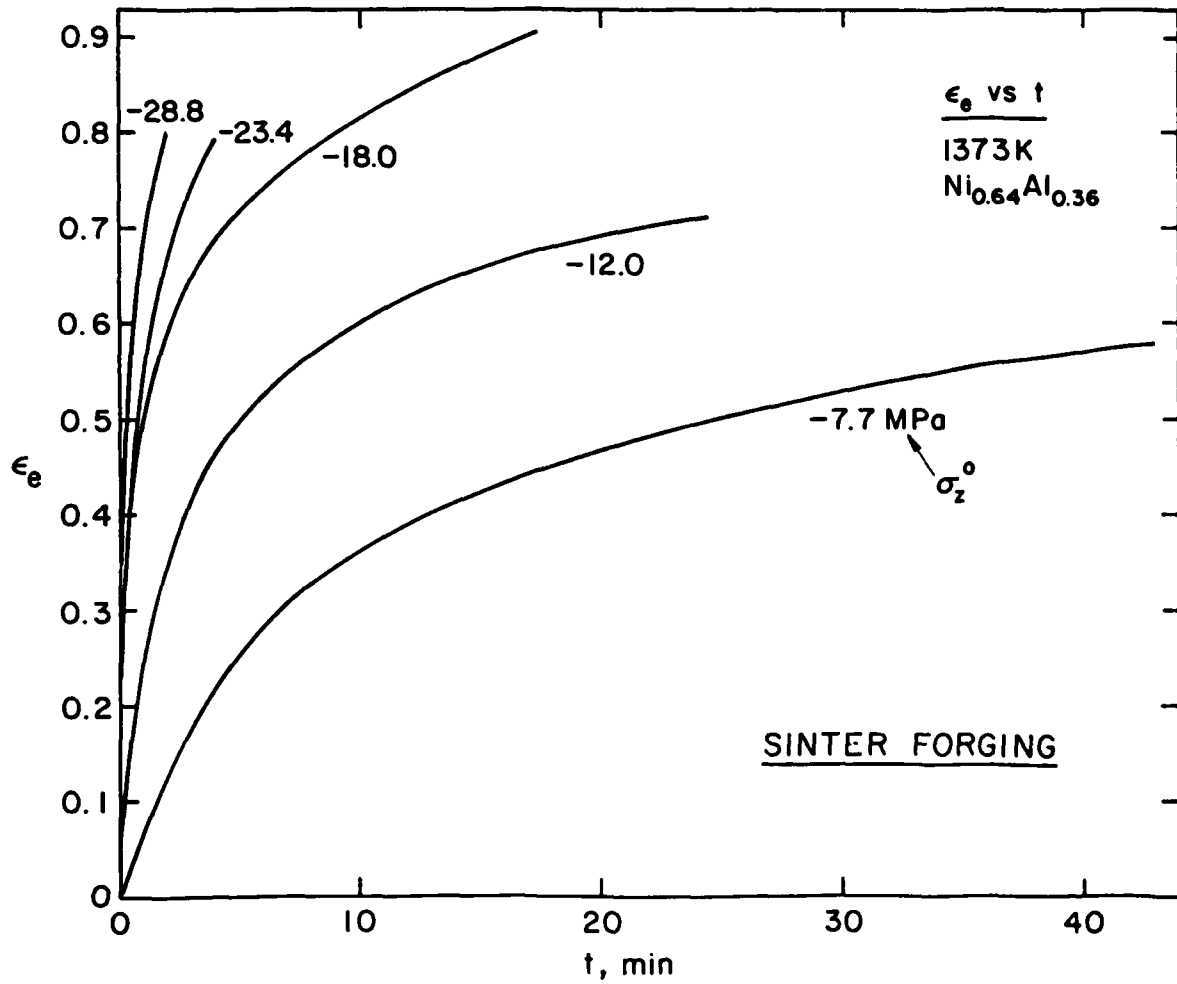
3. The axial strain as a function of time for the five sinter forging experiments. The stress is equal to the initial value of the applied stress, σ_z^0 . The experiments were carried out at constant load.



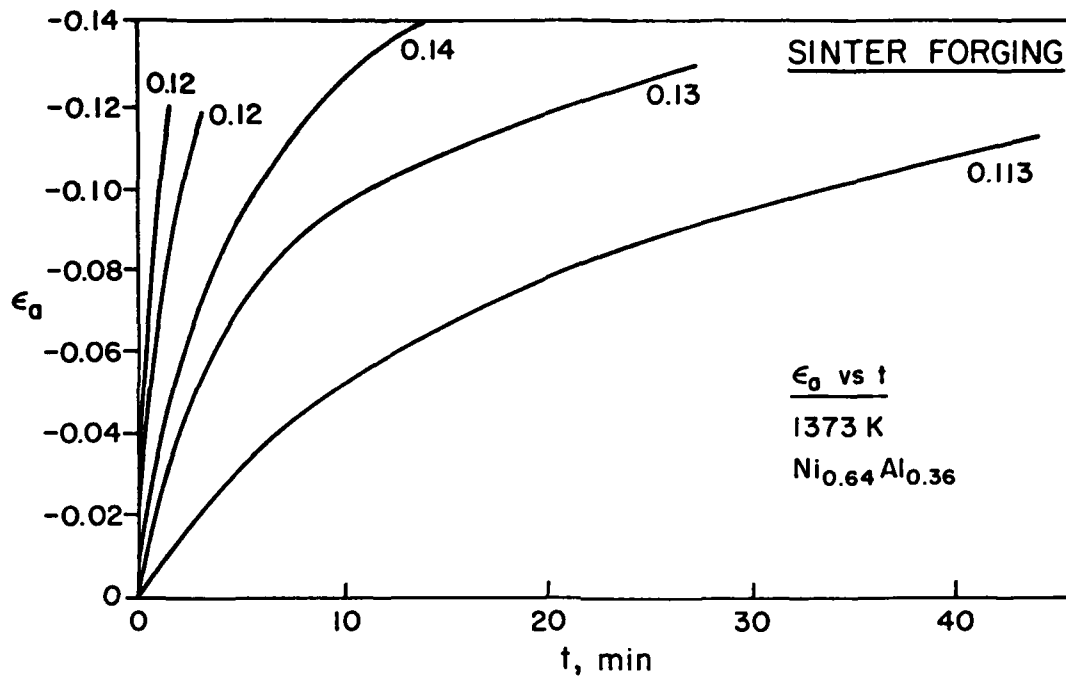
4. The radial strain as a function of time for the five sinter forging experiments. The stress is equal to the initial value of the applied stress, σ_z^0 . The experiments were carried out at constant load.



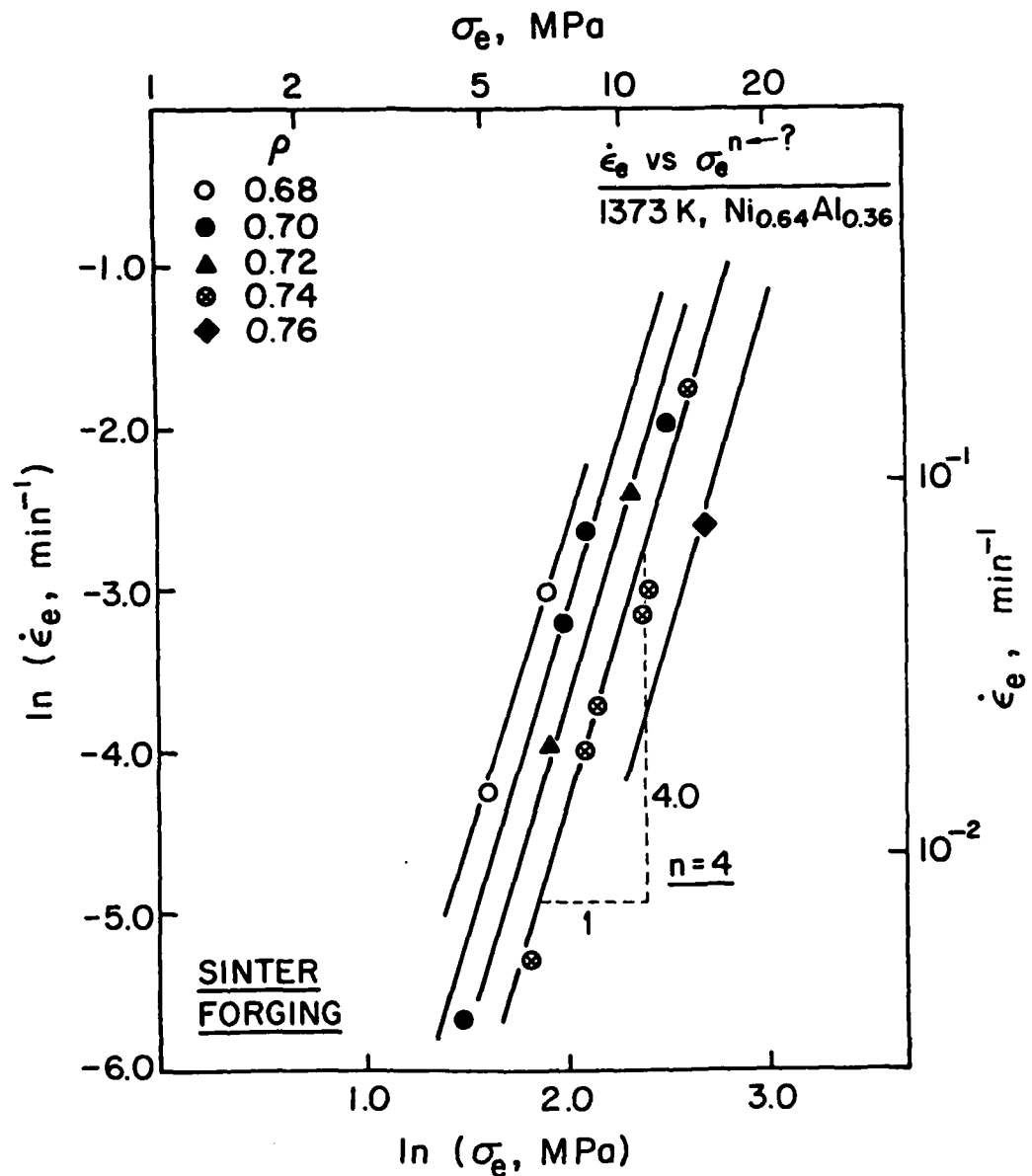
5. The true stress experienced by the specimens during the course of the five sinter forging experiments. The experiments were carried out at constant load.



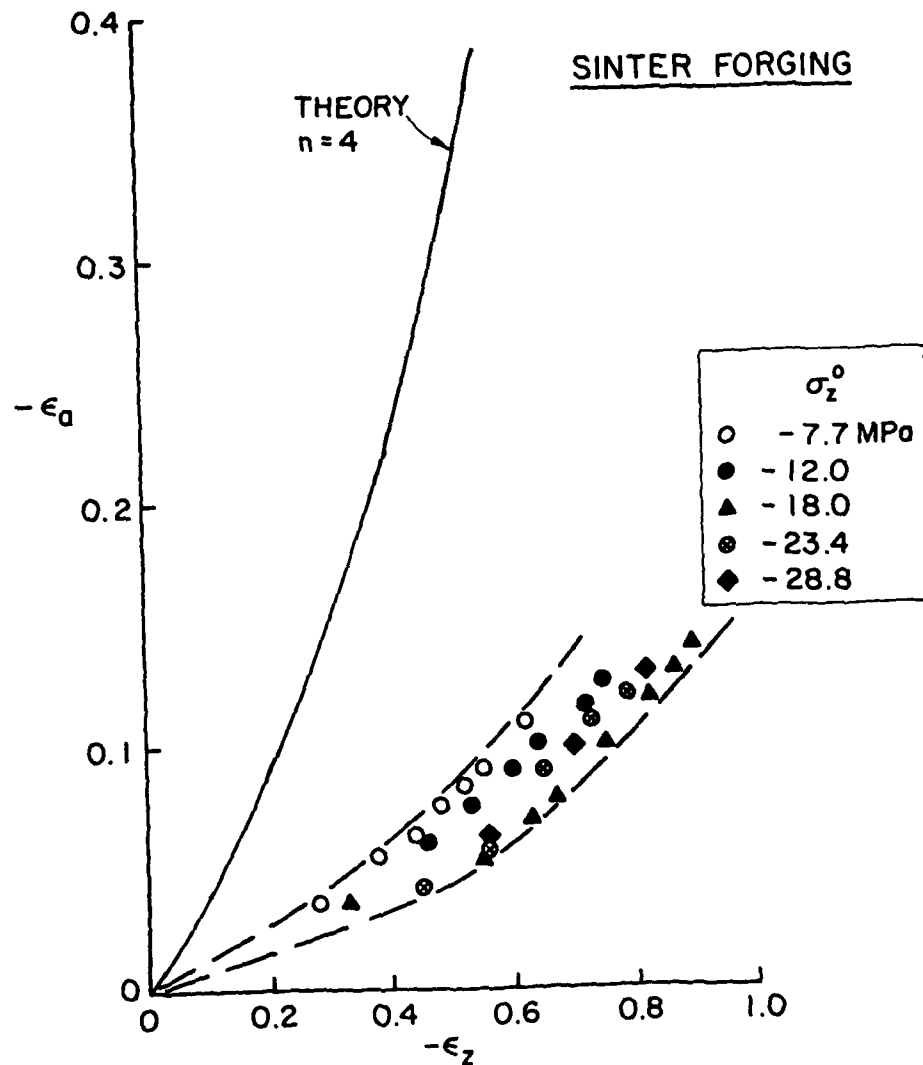
6. The effective strain, ϵ_e , as a function of time for the five sinter forging experiments.



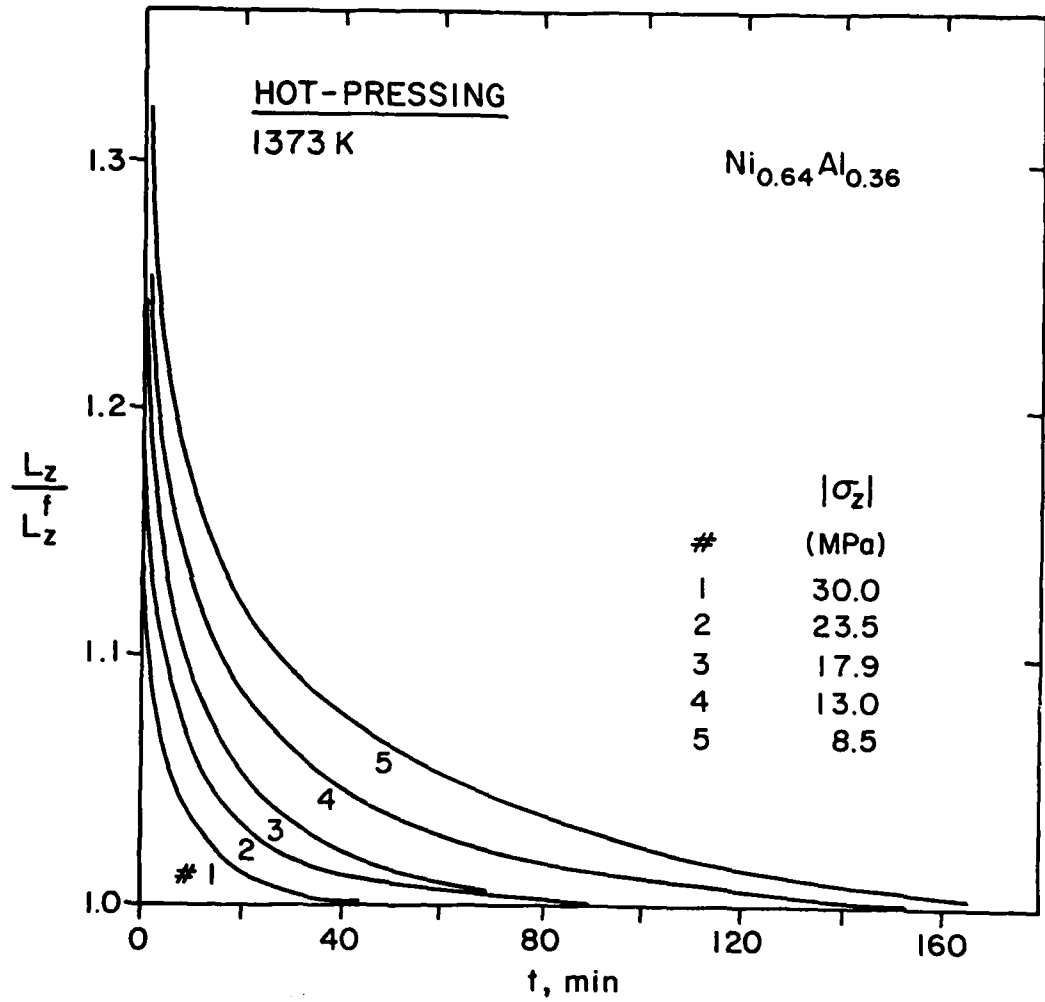
7. The volumetric strain, ϵ_a , as a function of time for the five sinter forging experiments.



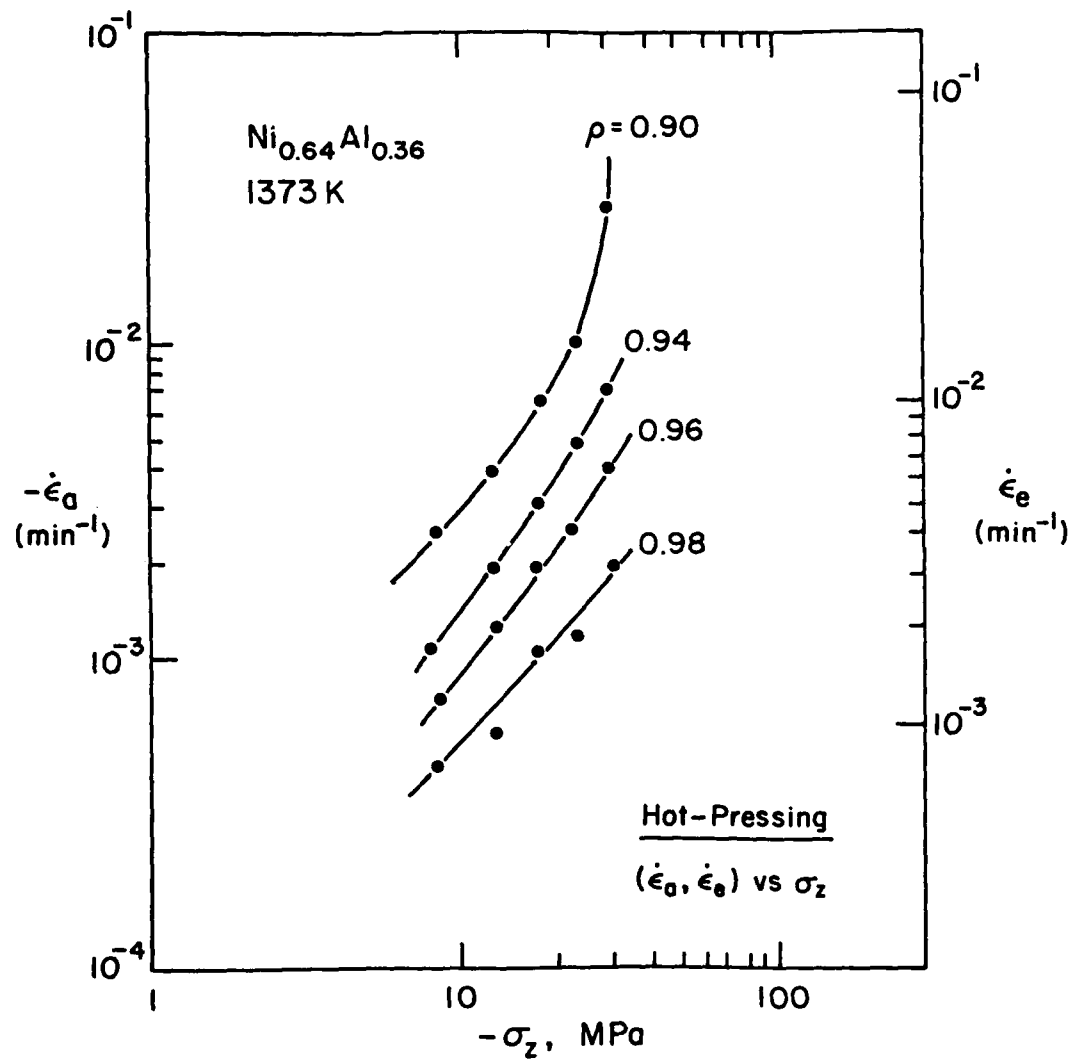
8. A logarithmic plot of $\dot{\epsilon}_e$ and σ_e to determine the value of the stress exponent for power law creep.



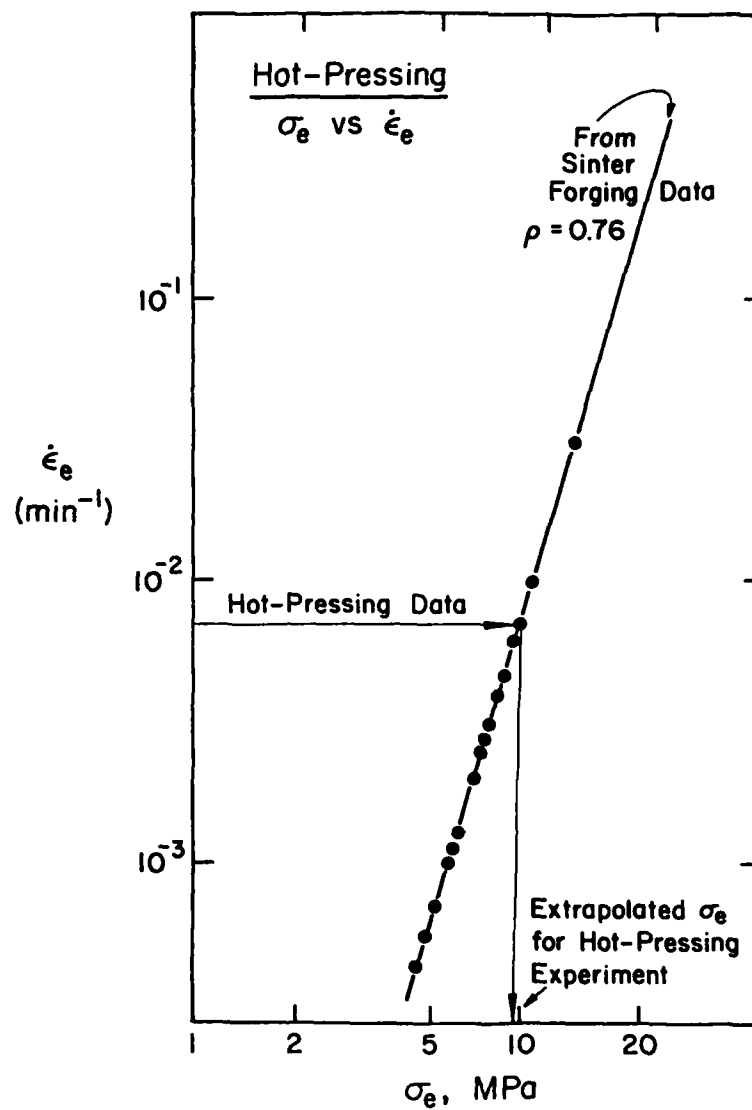
9. A comparison between the theoretical prediction and the measured rate of pore closure with applied axial strain. The theory greatly overestimated the closure rate of the pores.



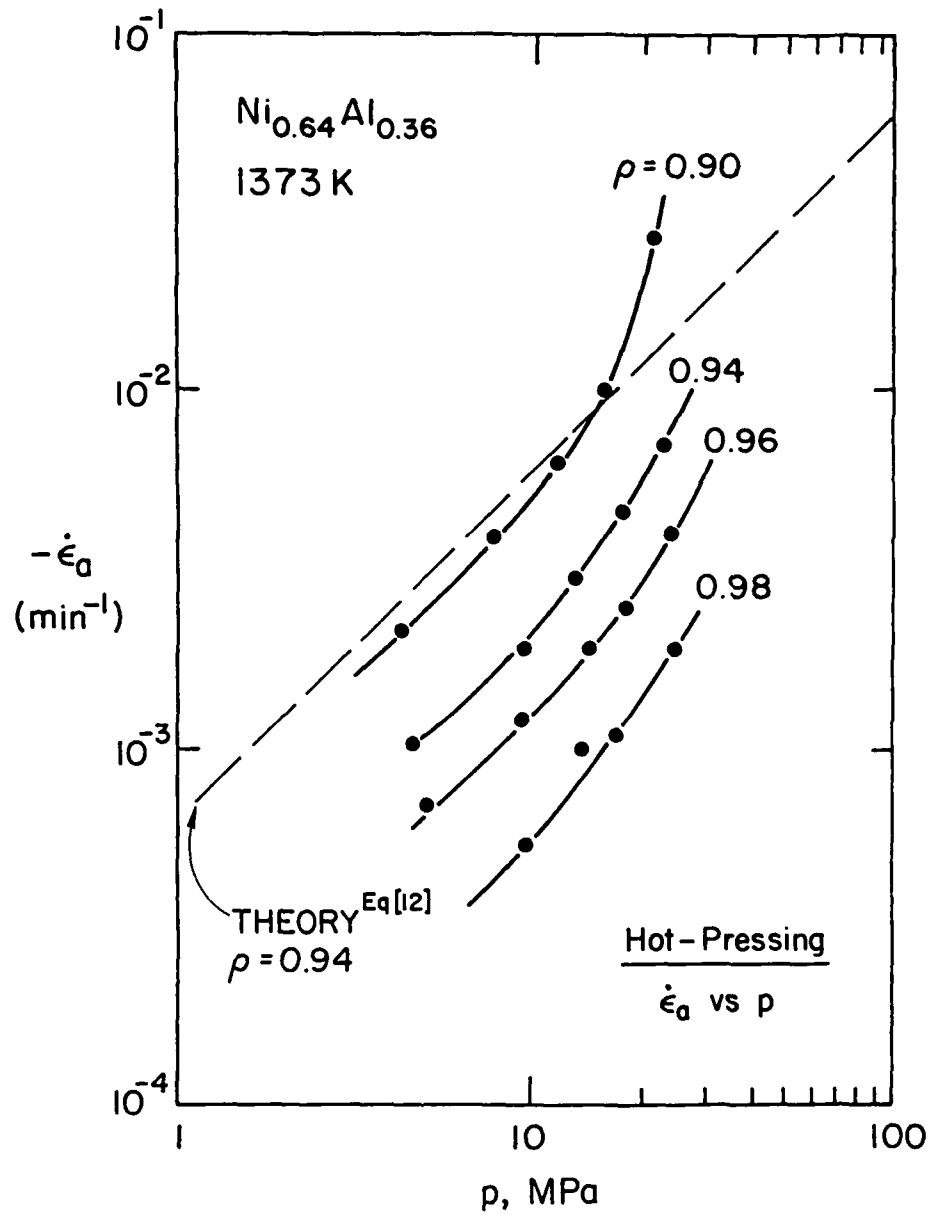
10. Data obtained from the five hot-pressing experiments. In hot-pressing the applied uniaxial stress remains constant since the specimen diameter does not change.



11. A plot of $\dot{\epsilon}_e$ and $\dot{\epsilon}_a$ as a function of the uniaxial stress, σ_2 . Note that the $\dot{\epsilon}_e$ is always two-thirds of $\dot{\epsilon}_a$.



12. The procedure used for obtaining the effective stress σ_e for the hot-pressing experiments by using $\sigma_e \sim \dot{\epsilon}_e$ data obtained from sinter forging experiments.



13. A plot of the volumetric strain rate $\dot{\epsilon}_a$ versus the applied pressure for hot-pressing experiments, and a comparison between theoretical prediction and experimental results.

Personnel

Graduate Students:

Joanne Beckman

John La Graff

K. R. Venkatachari

Technician:

Glenn Swan

Principal Investigator:

Rishi Raj

REPORTS AND PUBLICATIONS RESULTING FROM AFOSR FUNDING TO
Rishi Raj FROM 1973-1986

1. "Time Dependent Effects in Creep Fatigue," R. Raj, ASME MPC-3 Symposium of Creep Fatigue Interaction, New York 1976, p. 337-348.
2. "Mechanisms of Intergranular Fracture in High Temperature Fatigue," R. Raj, Materials Science Center Report #2843 (1977), prepared for the National Materials Advisory Board, National Academy of Sciences.
3. "A Mechanism of Intergranular Fracture During High Temperature Fatigue," B.K. Min and R. Raj, Fatigue Mechanisms, ASTM-STP (1979), Kansas City, pp. 569-591.
4. "The Effect of Cycle Shape on Creep Fatigue Interaction in Austenitic Stainless Steels," R. Raj and B.K. Min, ASME/Pressure Vessel and Piping Conf. (1978), Paper No. 78-pvp-89, Mechanical Engineering (1978), vol. 100, No. 11, p. 122.
5. "Interaction between Lattice and Grain Boundary Dislocations and their Role in Mechanical Properties of Interfaces," L.C. Lim and R. Raj, Journal de Physique, Colloque C4, Supplement au no. 4, Tome 46 (April 1985, pp. 581-595).
6. "The Evolution of Grain Size Distribution during Superplastic Deformation," A.K. Ghosh and R. Raj, Superplasticity, eds. B. Baudalet and M. Sirery, Editions du CNRS, Paris, 1985, pp. 11.1-11.19.
7. "Environmental Effects in Nickel-Base Alloys," S. Floreen and R. Raj, Flow and Fracture at Elevated Temperatures, ASM Materials Science Seminar, Amer. Soc. Metals, Metals Park, OH, 1985, pp. 383-406.
8. "Mechanisms of Creep Fatigue Interaction," R. Raj, Flow and Fracture at Elevated Temperatures, ASM Materials Science Seminar, Amer. Soc. Metals, Metals Park, OH, 1985, 215-250.
9. "On the Sintering Rate of Cleavage Cracks," R. Raj, W. Pavinich and C.N. Ahlquist, Acta Metallurgica (1975), vol. 23, p. 339.
10. "Use of the Internal Friction Technique to Measure Rates of Grain Boundary Sliding," Acta Metallurgica (1974), vol. 22, p. 1469.
11. "Transient Behavior of Diffusion Induced Creep and Creep Rupture," R. Raj, Metallurgical Transactions A (1975), vol. 6, p. 1499.
12. "Intergranular Fracture at Elevated Temperature," R. Raj and M.F. Ashby, Acta Metallurgica (1975), vol. 23, p. 653.

13. "Crack Initiation at Grain Boundaries under Conditions of Steady State and Cyclic Creep," Journal of Engineering Materials and Technology, R. Raj (1976), vol. 98, p. 132.
14. "De-Adhesion by Growth of Penney Shaped Bubbles in an Adhesive Layer," R. Raj and C.H. Dang, Philosophical Magazine (1975), vol. 32, p. 909.
15. "Measurement of Viscosity of the Grain Boundary Phase in Hot-Pressed Silicon Nitride," D.R. Mosher, R. Raj and R. Kossowsky, Journal of Materials Science (1976), vol. 11, p. 49.
16. "Fracture at Elevated Temperature," W. Pavinich and R. Raj, Metallurgical Transaction S (1977), vol. 8, p. 1917.
17. "Intergranular Fracture in Bicrystals," R. Raj, Acta Metallurgica (1978), vol. 26, p. 160.
18. "Correction to: Intergranular Fracture at Elevated Temperature," R. Raj, H.H. Shih and H.H. Johnson, Scripta Metallurgica (1977), vol. 11, p. 839.
19. "A New Method for Fatigue Testing at Room and Elevated Temperatures," Journal of Testing and Evaluation, American Society for Testing and Materials (1979), vol. 7, p. 24.
20. "Nucleation of Cavities at Second Phase Particles in Grain Boundaries," R. Raj, Acta Metallurgica (1978), vol. 26, p. 995.
21. "Hold-Time Effects in High Temperature Fatigue, Theory and Experiment," B.K. Min and R. Raj, Acta Metallurgica (1978), vol. 26, p. 1007.
22. "Diffusional Relaxation of Stress Concentration at Second Phase Particles," R.C. Koeller and R. Raj, Acta Metallurgica (1978), vol. 26, p. 1551.
23. "The Importance of Wedge Cracking in High Temperature Fatigue," B.K. Min and R. Raj, Canadian Metallurgical Quarterly (1979), vol. 18, p. 171.
24. "An Upper Bound in Strain Rate for Wedge Type Intergranular Fracture in Nickel During Creep," C. Gandhi and R. Raj, Metallurgical Transactions A (1981), March, vol. 12A, pp. 515-520.
25. "Creep Crack Growth by Cavitation Near Crack Tips," R. Raj and S. Baik, Metal Science Journal (1980), Aug/Sept. p. 385-3094.
26. "Stress Rupture," R. Raj and A.K. Ghosh, Metallurgical Transactions A (1981) July, vol. 12A, pp. 1291-1302.

27. "Micromechanical Modeling of Creep Using Distributed Parameters," R. Raj and A.K. Ghosh, Acta Metallurgica (1981) Feb., vol. 19, pp. 283-292.
28. "Grain Size Effects in Superplasticity," A.K. Ghosh and R. Raj, Acta Metallurgica (1981) May, vol. 29, pp. 607-616.
29. "Equations for Diffusional Creep under Multiaxial Loading," R. Raj, Scripta Metallurgica (1981), Feb., vol. 15, pp. 273-274.
30. "Intergranular Creep Fracture in Aggressive Environments," R. Raj, Acta Metallurgica (1982), vol. 30, pp. 1259-1268.
31. "Wedge Type Creep Damage in Low Cycle Fatigue," S. Baik and R. Raj, Metallurgica Transactions (1982), vol. 30, pp. 1207-1214.
32. "Mechanisms of Creep Fatigue Interaction," S. Baik and R. Raj, Metallurgica Transactions (1982), vol. 13A, pp. 1215-1221.
33. "The Effect of Environment on Grain Boundary Internal Friction in an Al-5% Mg Alloy," Acta Metallurgica (1982), vol. 30, pp. 499-503.
34. "Separation of Cavitation-Strain and Creep-Strain During Deformation," R. Raj, Journal American Ceramic Society (1982), vol. 65, No. 3, p. C-46.
35. "Correlations Between Cavitation, Creep and Dilation for Multiaxial Loading," R. Raj, Acta Metallurgica (1983), vol. 31, pp. 29-36.
36. "A Mechanism for Intergranular Fracture During High Temperature Fatigue," American Society for Testing and Materials, Special Technical Publication 675 (1979), pp. 569-591.
37. "Creep-Fatigue Interaction in OFHC-Copper," S. Baik and R. Raj, Scripta Metallurgica (1983), vol. 17, pp. 1087-1090.
38. "On Slip-Induced Intergranular Cavitation During Low-Cycle Fatigue of Nickel at Intermediate Temperature," L.C. Lim and R. Raj, Acta Metallurgica (1984), Vol. 32 (5), pp. 727-733.
39. "On the Distribution of Σ for Grain Boundaries in Polycrystalline Nickel Prepared by Strain-Annealing Technique," L.C. Lim and R. Raj, Acta Metallurgica (1984), Vol. 32, No. 8, pp. 1177-1181.
40. "Effect of Boundary Structure on Slip Induced Cavitation in Polycrystalline Nickel," L.C. Lim and R. Raj, Acta Metallurgica (1984), Vol. 32, No. 8, pp. 1183-1190.

41. "Continuity of Slip Screw and Mixed Crystal Dislocations across Bicrystals of Nickel at 573K," L.C. Lim and R. Raj, Acta Metallurgica (1985), Vol. 33, No. 8, pp. 1577-1583.
42. "The Role of Residual Dislocation Arrays in Slip Induced Cavitation, Migration and Dynamic Recrystallization on Grain Boundaries," L.C. Lim and R. Raj, Acta Metallurgica (1985), Vol. 33, No. 12, pp. 2205-2214.
43. "Slip-Twin Interactions in Bicrystals of Nickel at 573K at Large Strains," L.C. Lim and R. Raj, Scripta Metallurgica (1986), Vol. 20, pp. 539-544.
44. "Kinetics of Precipitation of α -Al₂O₃ Spinel Solid Solution," P.C. Panda and R. Raj, Journal of American Ceramic Society (1986), Vol. 69 (5), pp. 365-373.

END

8-87

DTIC